Journal of Rock Mechanics and Geotechnical Engineering 10 (2018) 635–644

Contents lists available at ScienceDirect

Journal of Rock Mechanics and Geotechnical Engineering

journal homepage: www.rockgeotech.org

Full Length Article

Shear properties of cemented rockfills

Bob A. Lingga, Derek B. Apel*

Department of Civil and Environmental Engineering, School of Mining and Petroleum, University of Alberta, Edmonton, Alberta T6G 1H9, Canada

ARTICLE INFO

Article history:
Received 12 February 2018
Received in revised form
11 March 2018
Accepted 28 March 2018
Available online 7 May 2018

Keywords:
Cemented rockfill (CRF)
Shear tests
Shear strength
Friction angle
Cohesion
Backfill interface

ABSTRACT

Application of cemented rockfilling to underground mining could not be separated from the corresponding backfill's shear strength properties. The shear of cemented rockfill (CRF)-rock wall and the shear interaction occurring within CRFs both have some disadvantageous failure chances. In this study, we tried to investigate the complete shear properties of CRFs using direct shear and triaxial tests of cemented granite rockfill. Large-scale triaxial testing was held to accommodate the large CRF sample. Direct shear testing on the prepared flat and smooth surfaces was assessed with brief conversions and their corrections were used to approximate the shear strength envelopes of CRF joint interfaces. Two types of CRFs with the same aggregate size and distribution but different unconfined compressive strengths (UCSs) due to different mixture designs indicated insignificant differences between their basic friction angles, and also their asperity inclination angles. Nevertheless, investigation between direct shear test and triaxial test showed that the specimen with higher UCS tended to have a slightly lower friction angle but a higher cohesion than the other one.

© 2018 Institute of Rock and Soil Mechanics, Chinese Academy of Sciences. Production and hosting by Elsevier B.V. This is an open access article under the CC BY-NC-ND license (http://creativecommons.org/licenses/by-nc-nd/4.0/).

1. Introduction

Backfill utilization has been increasingly reported for the recent underground mining sector. As economic resources are being found deeper due to the fact that the surface reserves are almost mined out, backfill utilization even incorporates binder materials such as cement in order to provide more strength. While a number of studies have been carried out on the compressive and tensile strengths of cemented backfills, studies on the shear properties and strength of backfills are rarely reported. In regard to the backfill as a stability support, it is argued that there is no really useful stability analysis for design if the shear strength of the product has been calculated incorrectly (Marachi et al., 1972).

In many Canadian underground mines, the use of cemented rockfill (CRF) as backfill material is a common practice (Yu and Counter, 1983; Reschke, 1993; Shrestha et al., 2008; Emad et al., 2012). Especially in cut-and-fill or blasthole stoping operations, which are usually divided by the primary and secondary stopes, shear properties play an important role (Sepehri et al., 2017a, b). While working on filling the primary stopes, shear interactions occur between the adjacent ore body or rock walls and the placed CRF. A number of studies have verified that stress interaction between the ore body and CRF may be mutually supported (Mitchell, 1989; Belem and Benzaazoua, 2008). On the other hand, mining advancements from the primary to the secondary stopes are supposed to exhibit shear interaction between the primary CRF and the placed CRF at the secondary stope. In this case, this experiment's purpose is to assess the CRF-CRF shear interaction.

Shear interaction in the presence of CRF can be separated into interface between CRF-CRF and interparticle of CRF by means of the mass. A case of sliding failure on the CRF's free-face during the adjacent ore extraction could be the shear interaction between interparticle and/or CRF mass. Fig. 1 shows the mining sequence where the shear interactions of CRF mostly take place.

In rock engineering practice, these two shear interactions are simply assumed to be the shear of discontinuity and shear of an unbroken material. Based on this, the direct shear and triaxial tests may be used to investigate the shear properties of CRF. It should be noted that this study treats CRF as a solid mass instead of loose aggregate accumulation. In this experiment, direct shear and triaxial tests were conducted on two different types of samples. Each sample was tested after 28 d of curing age. This time was selected so that the CRF should completely set and represent its optimum shear strength. Direct shear strength of CRF-CRF interface in this study is based on a flat and smooth surface approach.

* Corresponding author.
E-mail addresses: lingga@ualberta.ca (B.A. Lingga), dapel@ualberta.ca (D.B. Apel).
Peer review under responsibility of Institute of Rock and Soil Mechanics, Chinese Academy of Sciences.

https://doi.org/10.1016/j.jrmge.2018.03.005
1674-7755 © 2018 Institute of Rock and Soil Mechanics, Chinese Academy of Sciences. Production and hosting by Elsevier B.V. This is an open access article under the CC BY-NC-ND license (http://creativecommons.org/licenses/by-nc-nd/4.0/).

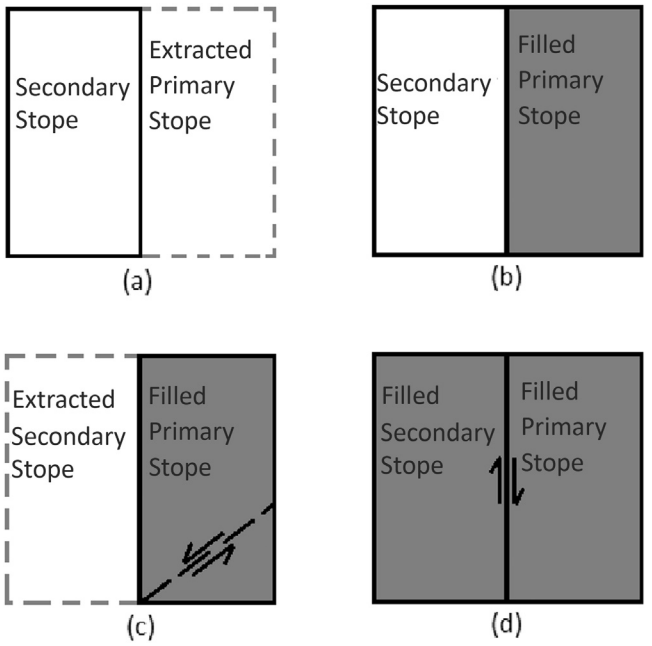

Fig. 1. Mining sequence: (a) primary stope mined, (b) primary stope after backfilling, (c) secondary stope mined and generated interparticle or CRF mass shear at exposed primary stope, and (d) secondary stope after backfilling with CRF-CRF interface shear interaction.

Samples in this study are laboratory-created CRF of granite aggregate rock retrieved from a diamond mine in Northern Canada.

The CRF incorporates a binder which, in setting the CRF, behaves more like concrete or rock than regular compacted or non-consolidated rockfill. This understanding is important to clarify Barton's shear strength criteria (Barton, 2013, 2016) that are used later in this study. Experimental work in this study follows Barton's shear strength of rock joints experiment instead of his shear strength of rockfill interfaces experiment, which is related to loose or non-cemented rockfill. Despite that the triaxial test of CRF is not commonly conducted due to the limited availability of a large triaxial cell for accommodating large CRF sample size, this study delivers the triaxial results of 152.4 mm (6 in) diameter CRF samples. Further details are given in the following sections.

2. Theory, material and experimentation

2.1. Shear strength criteria

Theoretically, a rock's shear strength can be expressed with the Coulomb relationship:

$$\tau = c + \sigma \tan \varphi \tag{1}$$

where τ, c, σ, and φ are the shear strength, cohesion, normal stress, and angle of internal friction, respectively. For rock joints, it is theoretically using the above equation without cohesion value, thus Eq. (1) for rock joints becomes

$$\tau = \sigma \tan \varphi \tag{2}$$

However, Eq. (2) only meets the criteria when any joint's contact is smooth, clean, and planar. Then, the generated shear strength envelope is supposed to be linear. However, in reality, any naturally occurring joint is most likely to undulate. In addition to the fact is that envelope plotting from the shear test is also nonlinear.

Various empirical approximations predicting the nonlinearity of a rock joint's shear strength envelope due to its naturally non-planar characteristics with curve-fitting were found to be more reliable. The initial attempts to interpret the shear strength of rough joints resulted in a bilinear model of shear strength envelope (Newland and Allely, 1957; Patton, 1966):

$$\tau = \sigma'_{\mathrm{n}} \tan(\varphi_{\mathrm{b}} + i) \tag{3}$$

where σ'_{n}, φ_{b}, and i are the effective normal stress, basic friction angle, and asperity inclination angle, respectively.

Patton (1966) configured the relationship using deviation of the shear strength envelope of a joint and φ_{b} plus i. The experiment of a wide range of normal stress variations toward a non-planar (artificially controlled undulation) interface sample resulted in a deviating shear envelope plot, in comparison with the smooth surface, which proved Patton's hypothesis.

Further development of the nonlinear shear strength envelope of a joint from bilinear to be more precise as curvilinear had been claimed (Barton, 1973, 1976, 2013, 2016; Barton and Choubey, 1977; Bandis et al., 1981; Barton and Bandis, 1982):

$$\tau = \sigma'_{\mathrm{n}} \tan\left[JRC\left(\log_{10}\frac{JCS}{\sigma'_{\mathrm{n}}}\right) + \varphi_{\mathrm{b}}\right] \tag{4}$$

$$\tau = \sigma'_{\mathrm{n}} \tan\left[JRC\left(\log_{10}\frac{JCS}{\sigma'_{\mathrm{n}}}\right) + \varphi_{\mathrm{r}}\right] \tag{5}$$

$$\tau = \sigma'_{\mathrm{n}} \tan\left[JRC_{\mathrm{n}}\left(\log_{10}\frac{JCS_{\mathrm{n}}}{\sigma'_{\mathrm{n}}}\right) + \varphi_{\mathrm{r}}\right] \tag{6}$$

where JRC is the joint roughness coefficient, JCS is the joint-wall compression strength, JCS_{n} and JRC_{n} are respectively the corrected JCS and JRC based on the length of observed joint, and φ_{r} is the residual friction angle.

In Eq. (4), JRC and JCS are the first two terms introduced by Barton in his earlier study. Upon the development, in consideration of weathering of the natural joint and the difference between a prepared flat surface and natural surface due to residual shear, Barton and Choubey (1977) substituted φ_{b} in Eq. (4) with φ_{r} as given in Eq. (5). Further, Eq. (6) was developed by Bandis et al. (1981) after Barton and Choubey (1977), where JRC_{n} and JCS_{n} were used to take into account the field scale effect, rather than the derivatives of JRC and JCS.

Barton (2013) suggested that the curvilinearity of the shear strength envelope was affected by how rock behaves under the stress applied. A series of triaxial tests indicated the brittle-ductile behavior of rock as elastoplastic material bended the shear strength envelope (see Fig. 2).

Zhao (1997) proposed an equation (Eq. (7)) based on Barton-Choubey's model (Eq. (5)) by adding a correction factor of interface matching factor or joint matching factor (JMC) to the JRC. He considered the field condition when usually the joint interface was not completely matching as a fresh joint. Therefore, he also used the term residual friction angle instead of basic friction angle.

$$\tau = \sigma'_{\mathrm{n}} \tan\left[(JMC)(JRC)\left(\log_{10}\frac{JCS}{\sigma'_{\mathrm{n}}}\right) + \varphi_{\mathrm{r}}\right] \tag{7}$$

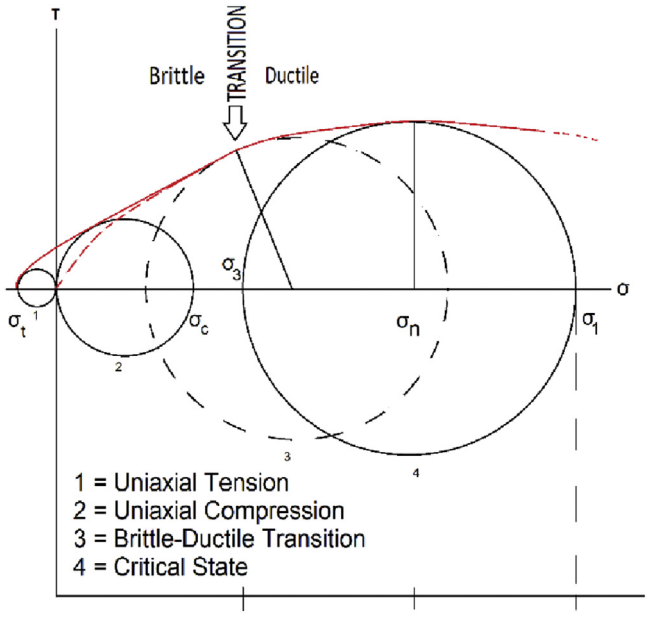

Fig. 2. Bending of shear strength envelope due to brittle-ductile transition obtained from triaxial tests result (after Barton, 2013).

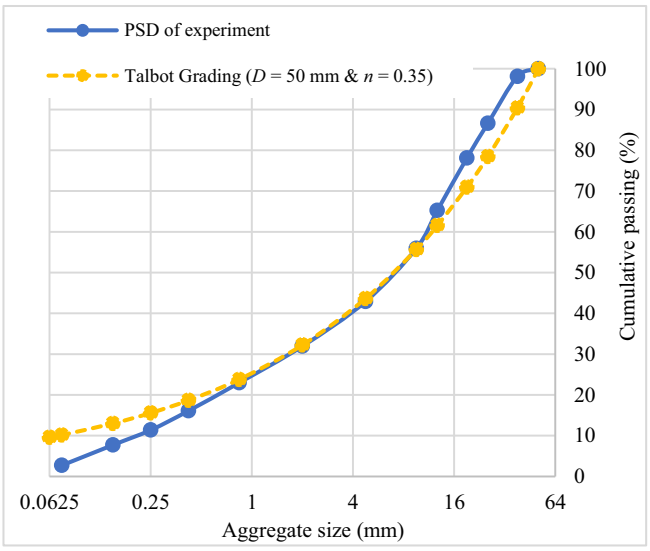

Fig. 3. PSD analysis result of the aggregate source.

2.2. CRF samples

Granite aggregate of maximum 50.8 mm (2 in) in this context as the material source was going through particle size distribution (PSD) analysis. In mining practice, any particle size larger than 10 mm is generally defined as coarse aggregate. In this instance, this experimental aggregate consists of 40% coarse and 60% fine aggregate by weight. Fig. 3 shows the aggregate size gradation that fits Talbot and Richart (1923) suggested method modified by Swan (1985) for determining the cemented backfills' particle distribution, with the exponent value (n) of 0.35.

The CRF mixtures were identified by different proportions of water to cement and the cement content. Like the CRF commonly used in the field, experimentally reproduced CRF used general Portland cement as a binder and also admixture adding. General Portland cement type 10 and admixture MasterSet Delvo were selected. Table 1 lists the detail of these two experimental CRF mixtures in weight.

To meet the standard sample size regarding the nominal maximum aggregate size, the mold with dimension of diameter × length of 152.4 mm × 304.8 mm (6 in × 12 in) was used (ASTM C192/C192M, 2016). Prepared samples for the triaxial test were then stored at the moisture chamber with relative humidity of 95%–100% and temperature of (25 ± 2) °C; while the samples for the direct shear test were placed indoors. The purpose of dry-cured direct shear samples was to mimic the field condition when joints are mostly dry due to air exposure. As suggested by Barton (1976), the surface condition for the test may be dry or wet according to the desired application, and Zhao (1997) also did his experiment with dry samples.

2.3. Load frame and experimentation

2.3.1. Triaxial apparatus and testing

In the Rock Mechanics Laboratory, University of Alberta, a specially fabricated 152.4 mm (6 in) diameter Hoek triaxial cell by RocTest (2017) was used to accommodate triaxial samples in this study. The loading frames incorporated a 10,000 kN capacity servo-hydraulic INSTRON machine to generate the axial load and a syringe hydraulic pump ISCO Model 100DX to provide the confining pressure. Data gathered from the test were recorded by a data acquisition system. Fig. 4 shows the triaxial cell on the loading frame used in the experiment.

The experiment generally followed the standard method A (ASTM D7012-14, 2014). The test was run on a controlled rate of 0.3 mm/min of axial displacement until the sample failed. Three samples of CRF-1 and CRF-2 each were tested under different confining pressures.

2.3.2. Direct shear testing and apparatus

The test utilized the Golder Association direct shear machine with constant normal load (CNL) (Hencher and Richards, 1982) in the same laboratory (see Fig. 5). The machine incorporated one linear position (LP) transducer for normal displacement, two LP transducers for shear displacement, and one pressure transducer for the shear stress. The two horizontal LP transducers were each placed at one side of the yoke. Test results of three LP transducers and one pressure transducer were automatically recorded by the data acquisition system.

With respect to the limited dimensions of the shear box apparatus, all direct shear samples were further prepared to fit the shear box. Dry-cured cylindrical samples were then cut to be rectangular bars with a 78 mm × 127 mm flat and smooth contact area. The shear direction traveled along the longest cross-sectional dimension. Following the standard (ASTM D5607-16, 2016) that 10 times of the

Table 1
CRFs mix designs.

Mix type	Aggregate size of waste rock (mm)	Cement to aggregate ratio (%)	Water to cement ratio	Water to solid ratio	Admixture Delvo (L/100 kg cement)	Density (kg/m^3)	Dry density (kg/m^3)
CRF-1	<50	4.5	2	0.087	0.475	2358.089	2191.442
CRF-2	<50	10.5	1	0.096	0.675	2507.667	2345.741

Fig. 4. The 154.2 mm diameter Hoek triaxial cell and 10,000 kN capacity loading frame INSTRON.

maximum asperity height along the shear surface should be the minimum of the least cross-sectional areas, the experiment's prepared smooth and flat sample's interface (i.e. with asperity height approaching zero) should satisfy. Bonding the specimen to the shear box was utilizing the plaster of Paris as the encapsulating material.

The experiment used the multistage direct shear test with the repositioning procedure to create three plots of shear-normal stress paths from each of the two samples of CRF-1 and CRF-2. The decreasing nominal contact area was taken into account in calculation of the effective stress due to the increasing shear displacement in each test or the catastrophic damages from the previous test-stage. The expected experimental results are illustrated in Fig. 6. Similar approach for rock joints direct shear test in the laboratory was used by Muralha et al. (2014), indicating a slight increase of shear stress along each test-stage as the effect of decreasing contact area. The particular procedure suggested that at least three and preferably more normal stresses (F_n) should be applied for a single joint.

3. Results and discussion

3.1. Interparticle shear strength of CRF

A set of triaxial tests was conducted for a total of eight samples, four samples of each CRF (i.e. CRF-1 and CRF-2). The first test on each sample was set without a confining pressure to get the UCS (σ_c) of corresponding CRF type. The test results, σ_c, of CRF-1 and CRF-2 were 3.39 MPa and 9.22 MPa, respectively. The σ_c was also used as the confining pressure (σ_3) of next triaxial tests, as the σ_3 value of the following triaxial tests was supposed to not exceed 45%

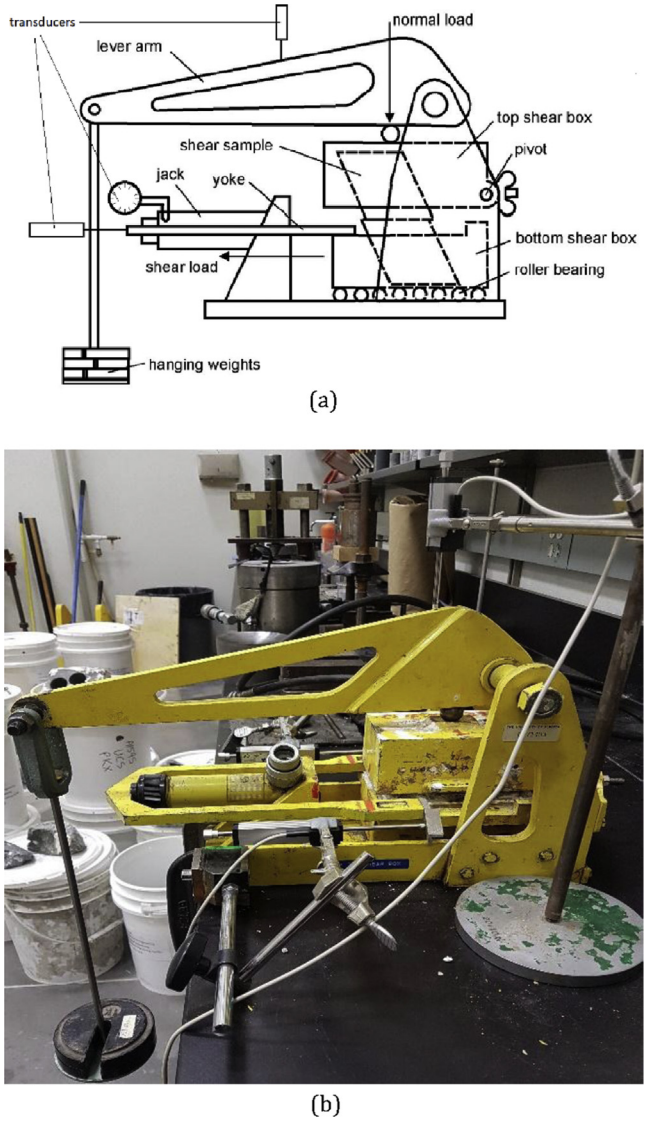

Fig. 5. Direct shear machine: (a) schematic, and (b) actual direct shear apparatus.

of the σ_c value. In addition, σ_c was also used as the JCS value of Barton's shear strength input in the next section of this study. Table 2 shows the results of triaxial tests of the experiment. Further, the CRF interparticle shear strength envelope is generated with the Coulomb relationship based on Eq. (1) using RocData 5.0 software.

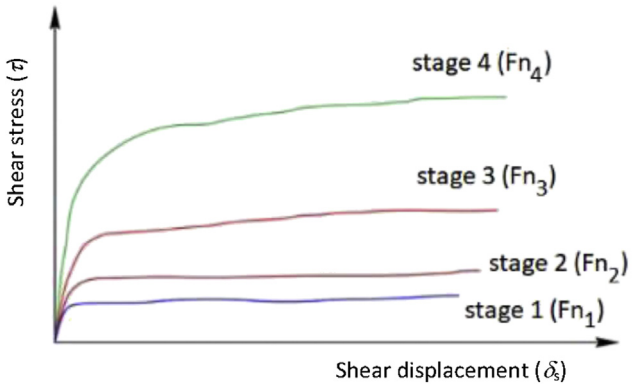

Fig. 6. Example of multi-stage shear test under different CNLs with repositioning after Muralha et al. (2014).

Table 2
Triaxial test results data.

Method	No. of test	CRF-1					CRF-2				
		σ_3 (MPa)		σ_1 (MPa)	c (MPa)	φ (°)	σ_3 (MPa)		σ_1 (MPa)	c (MPa)	φ (°)
		Set	Actual				Set	Actual			
Specimen test	1	0	0	3.39			0	0	9.22		
	2	0.75	0.74	8.55			1.5	1.49	19.41		
	3	1	1.05	10.93			2.5	2.57	22.24		
	4	1.5	1.49	12.16			3.5	3.49	28.25		
RocData 5.0					0.76	45.9				2.16	42.78

The software is used to best fit the shear strength envelope of each CRF (see Fig. 7).

Best-fit cohesions and angles of internal friction from RocData are then put into Eq. (1) to model the Coulomb relationship of both shear strength envelopes of interparticle CRF as follows:

$$\tau_{\text{CRF-1}} = 0.76 + \sigma \tan 45.9^{\circ} \tag{8}$$

$$\tau_{\text{CRF-2}} = 2.16 + \sigma \tan 42.78^{\circ} \tag{9}$$

The triaxial result assessed with the Coulomb relationship for the CRF gives an understanding of interparticle shear strength of CRF-1, which has cohesion (c) of 0.761 MPa and angle of internal friction (φ) of 45.9°; CRF-2 has c value of 2.163 MPa and φ value of 42.78°. For the same aggregate size and proportion but different material strengths, it is indicated that CRF-1 has a slightly higher angle of internal friction than CRF-2, but CRF-1 has a lower cohesion compared with CRF-2.

Fig. 8 shows the failure angle resulting from the experiment. The CRF-1 sample is shown on the left and the CRF-2 is on the right side of this figure. It suggests that the failure mode of CRF under the shear triaxial test indicates a high angle of failure plane. The high angle of failure plane occurs not only to CRF-1 but also to CRF-2.

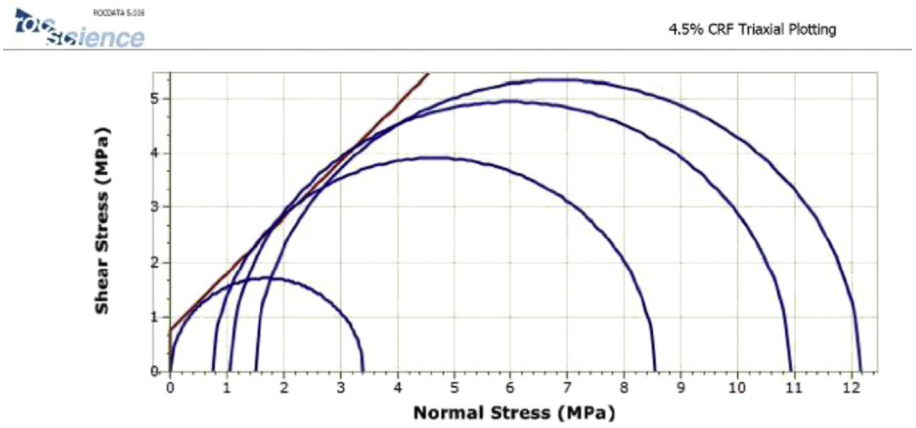

(a) CRF-1.

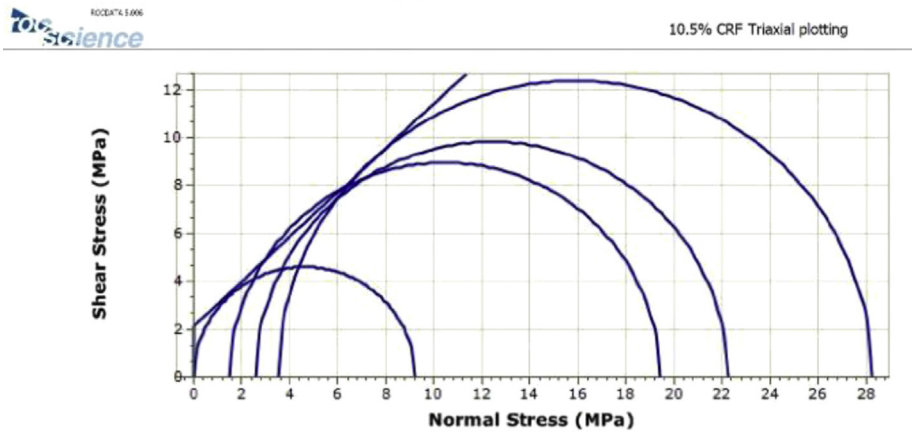

(b) CRF-2.

Fig. 7. Interparticle shear strength envelopes of CRF-1 and CRF-2 by RocData.

Fig. 8. Mode of failure of CRF under triaxial test.

3.2. Interface shear strength of CRF-CRF

The three stages of direct shear tests with the applied normal loads are 1 kN, 1.6 kN, and 2 kN, respectively, which are applied to the four direct shear samples. Generated normal loads from the hanging weights are assumed given the uniform normal load to the nominal area throughout the test. The plots of shear stress-displacement are shown in Fig. 9. The resulted plots are very similar to the work of Muralha et al. (2014) (see Fig. 6). Fig. 10 shows the plotting of shear strength envelopes from direct shear test results.

Thus, the shear strength envelopes of the flat and smooth interfaces of CRF-CRF based on Eq. (2) in terms of σ'_n and φ_b are written as.

$$\tau_{CRF\text{-}1} = \sigma'_n \tan \varphi_{b1} \text{ or } \tau_{CRF\text{-}1} = \sigma'_n \tan 39.91^\circ \quad (10)$$

$$\tau_{CRF\text{-}2} = \sigma'_n \tan \varphi_{b2} \text{ or } \tau_{CRF\text{-}2} = \sigma'_n \tan 41.83^\circ \quad (11)$$

In this study, the assessment of Patton and Barton's shear strength criteria was approximated from the artificial tension fracture of corresponding CRF. Considering the nature of the particular CRF, binder-aggregate bonding in granite CRF was assumed weaker than the granite aggregate itself. This assumption was confirmed by the UCS tests conducted on the same CRF and granite samples composing the aggregate component of the testing backfill mixture. The UCS value of tested granite core samples was approximately 120 MPa, while the CRF-1 and CRF-2 had UCS values of around 3–9 MPa. Therefore, the shear failure of the CRF material creates fracture with surface profile where the fracture goes through the cementitious bond but only follows the outline of the granite aggregate pieces. Based on our observations regardless of failure mode, the surface profiles of fractured CRF material are very similar. Therefore, the tested CRF profiles can be obtained using the split tensile concrete cylinder procedure in accordance with the standard (ASTM C496/C496M, 2017). The natural joint of granite CRF may be identical to the artificial tension fracture, thereby satisfying with CRF-CRF interfaces as well.

A set of asperity inclination angle (i) measurements was recorded using the profile gage. Then they were captured and computed using the software MB-Ruler to give more precise angle values (see Table 3 and Fig. 11). The average i value was back-calculated for each CRF to model Patton's shear strength criterion. Combining the average i value with basic friction angle of each CRF from Eqs. (10) and (11) gave Patton's shear strength of CRF-CRF interfaces in Eqs. (12) and (13):

$$\tau_{CRF\text{-}1} = \sigma'_n \tan(\varphi_{b1} + i_1) \text{ or } \tau_{CRF\text{-}1} = \sigma'_n \tan 72.14^\circ \quad (12)$$

$$\tau_{CRF\text{-}2} = \sigma'_n \tan(\varphi_{b2} + i_2) \text{ or } \tau_{CRF\text{-}2} = \sigma'_n \tan 71.96^\circ \quad (13)$$

In the Patton's model, Eqs. (12) and (13) are basically the first part of the linear envelope of each CRF type, while Eqs. (10) and (11) are the second part of the linear envelope. This CRF-CRF "smooth and planar interface" experiment indicates a limitation in modeling Patton's bilinear shear strength criterion in terms of the intersection point between the two linear envelopes determination (see Fig. 12). Nevertheless, this direct shear of smooth and planar together with tensile fracture asperity inclination measurements of CRF-CRF interface can still produce φ_b and i. Patton's experiment claimed that φ_r was compared favorably with φ_b (always within 1.5° of φ_b) and both were often identical, while the study of CRF attempted to model the φ_r with Barton and Choubey's φ_r estimation using

$$\varphi_r = (\varphi_b - 20) + 20(r/R) \quad (14)$$

where r and R are the Schmidt rebound numbers on wet joint surfaces and dry flat-smooth surfaces, respectively.

A set of Schmidt rebound number measurements were conducted using an L-type PROCEQ concrete Schmidt hammer and followed by averaging the highest five data as suggested by Barton and Choubey (1977) and Barton (2013, 2016) (see Table 4). The corrections for the average r and R values of CRF-1 were both 10. Because of the particular test on CRF-1, neither r nor R could reach the smallest rebound number on the Schmidt (i.e. 10). Calculated using Eq. (14), the residual friction angles of CRF-CRF interfaces are

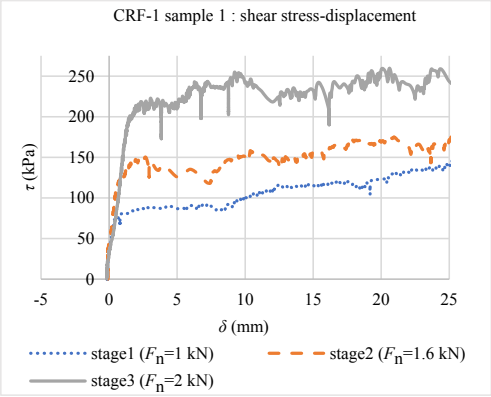

(a) CRF-1 sample 1.

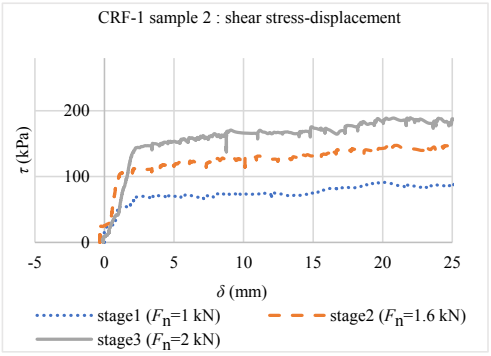

(b) CRF-1 sample 2.

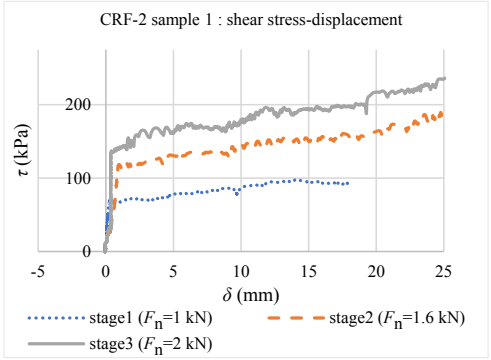

(c) CRF-2 sample 1.

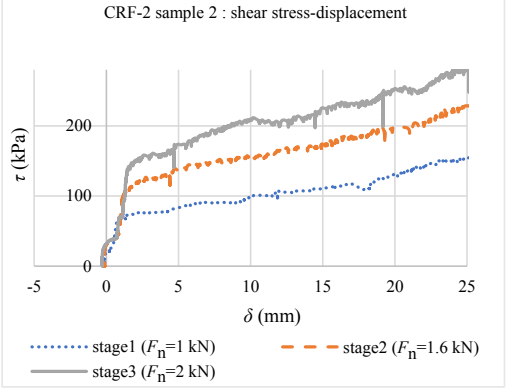

(d) CRF-2 sample 2.

Fig. 9. Shear stress-displacement curves of CRF-1 and CRF-2 samples.

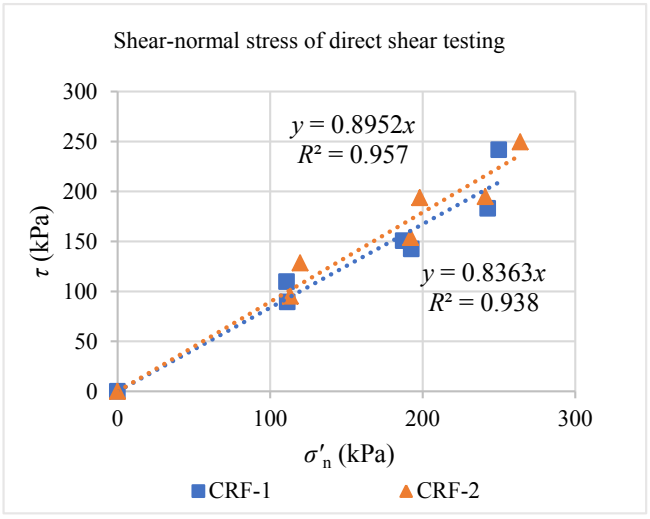

Fig. 10. Shear strength envelopes of flat and smooth CRF-CRF interfaces.

Table 3
Measurement data of *i* angle (°).

No. of test	CRF-1			CRF-2		
	Min.	Max.	Mean	Min.	Max.	Mean
1	21.38	65.39	43.38	9.42	54.98	32.2
2	7.79	49.21	28.5	5.53	28.59	17.06
3	11.97	30.79	21.38	16.45	41.49	28.97
4	23.65	54.62	39.14	24.15	28.94	26.54
5	23.84	55.1	39.47	9.53	45.44	27.48
6	24.02	43.47	33.74	12.39	37.81	25.1
7	15.77	63.07	39.42	9.61	57.59	33.6
8	9.61	43.97	26.79	18.81	40.31	29.56
9	13.9	56.9	35.4	7.64	58.64	33.14
10	8.57	30.58	19.58	15.58	32.09	23.84
11	10.96	44.56	27.76	15.59	34.78	25.18
12	18.19	30.31	24.25	9.21	70.13	39.67
13	11.34	43.02	27.18	12.64	66.34	39.49
14	20.55	64.69	42.62	15.38	58.96	37.17
15	11.35	58.36	34.86	13.05	52.85	32.95
Average			32.23			30.13

$$\varphi_{r,CRF\text{-}1} = 39.91^\circ \tag{15}$$

$$\varphi_{r,CRF\text{-}2} = 37.07^\circ \tag{16}$$

The estimation of JRC was assessed using a surface profiler to interpret the artificial tension fracture's profile of both CRFs, by matching them into available graphic and chart methods (Barton and Choubey, 1977). The result simply gave a JRC of 20 (maximum value). A JRC value of 20 for this experiment seemed obviously to consider the joint surfaces consisting of 50.8 mm or less coarse aggregates. Fig. 13 illustrates the coarse nature of the placed CRF in the field.

The JCS estimation was assumed equal to the σ_c value. Therefore, combinations of residual friction angles (i.e. Eqs. (15) and (16)), JRC values, and JCS values created Barton's shear strength of CRF-CRF interfaces as (where τ and σ'_n are in MPa):

$$\tau_{CRF\text{-}1} = \sigma'_n \tan\left(20 \log_{10}\frac{3.39}{\sigma'_n} + 39.91^\circ\right) \tag{17}$$

Fig. 11. The i measurement using profiler.

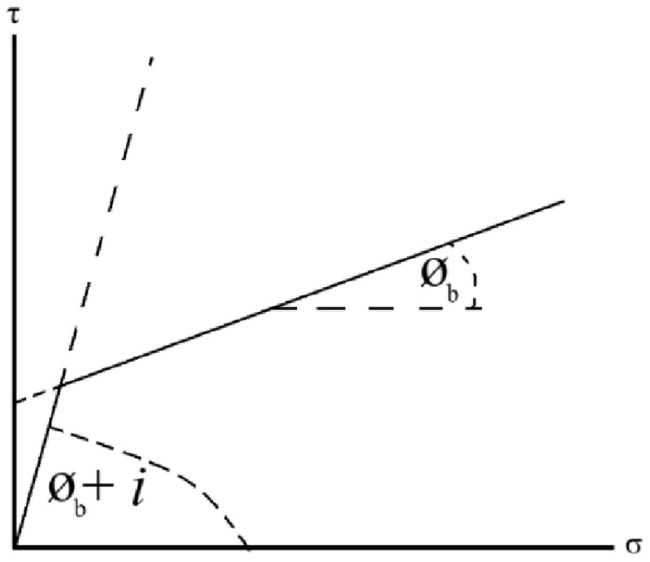

Fig. 12. Patton's bilinear shear strength envelope.

$$\tau_{\text{CRF-2}} = \sigma'_{\text{n}} \tan\left(20 \log_{10}\frac{9.22}{\sigma'_{\text{n}}} + 37.07^{\circ}\right) \quad (18)$$

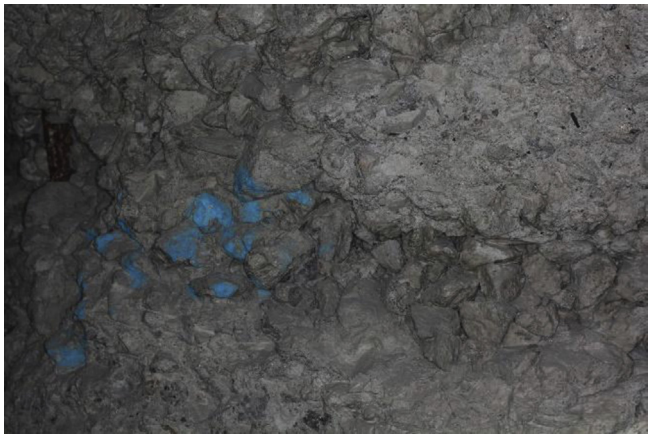

Fig. 13. Backfill underground stope with the laboratory tested CRF showing typical rough and undulating surfaces.

Fig. 14 shows the extrapolation of Barton's shear strength envelopes of CRF-CRF interfaces in this study. The plot is extrapolated by using Eqs. (17) and (18).

Barton's shear strength assessment shows that the CRF-1 envelope yields earlier than CRF-2, i.e. CRF-1's transition zones are surpassed earlier than CRF-2 in the same effective normal stress state. In simple terms, CRF-2 is stronger than CRF-1. In the previous Patton's shear strength assessment, however, it is impossible to determine which CRF type has higher shear strength because intersection points could not be determined when φ_{b} and i were almost identical.

The situation is understandable because Barton's shear strength criterion is highly affected by JCS since the logarithmic function has to be multiplied by JRC. CRF-1 has JCS around one-third of CRF-2's JCS (for CRF-1, $\sigma_{\text{c}} = JCS = 3.39$ MPa; for CRF-2, $\sigma_{\text{c}} = JCS = 9.22$ MPa). Even when φ_{r} and JRC are not significantly differed, Barton's shear strength criteria and procedure are able to model the shear strength of the CRF-CRF interface from only the direct shear of smooth and planar surface testing.

Analysis of the basic and the residual friction angle differences of the CRF-1 experiments confirms with Patton's experiment where φ_{r} and φ_{b} are identical, although in the case of CRF-2, φ_{r} differs from φ_{b} at around 4.75° which is slightly off from 1.5°. It can be concluded that for granite CRF, φ_{r} and φ_{b} are likely not similar to each other.

A comparison between triaxial test results and direct shear test results are shown in Table 5. The experimental result confirms that the Barton's shear strength assessment is successful in describing

Table 4
Schmidt rebound number measurement data.

No. of test	CRF-1						CRF-2					
	r			*R*			*r*			*R*		
	Set 1	Set 2	Set 3	Set 1	Set 2	Set 3	Set 1	Set 2	Set 3	Set 1	Set 2	Set 3
1	≤10	≤10	≤10	≤10	≤10	≤10	10	10	10	10	14	10
2	≤10	≤10	≤10	≤10	≤10	≤10	11	12	11	11	16	11
3	≤10	≤10	≤10	≤10	≤10	≤10	11	13	11	15	17	14
4	≤10	≤10	≤10	≤10	≤10	≤10	11	13	12	16	17	15
5	≤10	≤10	≤10	≤10	≤10	≤10	11	14	12	20	20	16
6	≤10	≤10	≤10	≤10	≤10	≤10	14	15	12	20	20	18
7	≤10	≤10	≤10	≤10	≤10	≤10	15	15	13	20	21	18
8	≤10	≤10	≤10	≤10	≤10	≤10	18	17	14	20	22	18
9	≤10	≤10	≤10	≤10	≤10	≤10	18	19	16	22	23	22
10	≤10	≤10	≤10	≤10	≤10	≤10	22	19	20	22	26	30
Average of highest 5	10	10	10	10	10	10	17	17	15	21	22	21
Average	10			10			16			21		

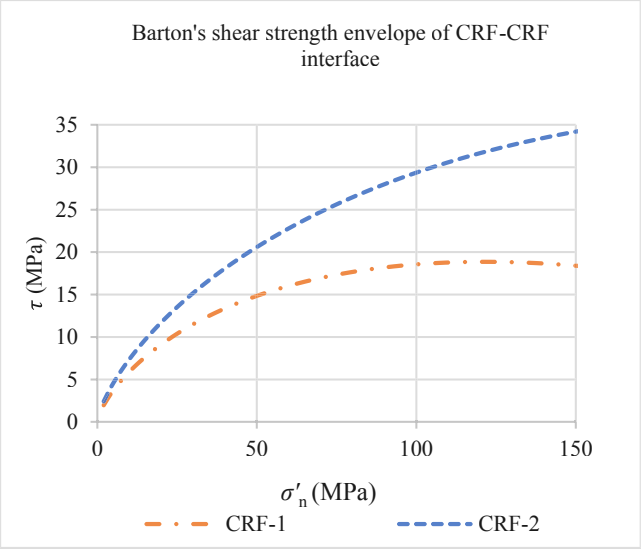

Fig. 14. Barton's shear strength envelopes of CRF-CRF interfaces.

Table 5
The shear properties of granite CRFs.

CRF	Triaxial test		Direct shear test		
	c (MPa)	φ (°)	φ_r (°)	φ_b (°)	$\varphi_b + i$ (°)
CRF-1	0.76	45.9	39.91	39.91	72.14
CRF-2	2.16	42.78	37.07	41.83	71.96
Criterion	Coulomb		Barton	Patton	

CRF shear property similarly with the triaxial test. The shear strength of CRF-2 is higher than that of CRF-1 (in the triaxial test, it is indicated by the higher cohesion; in Barton's test, it is indicated by the higher envelope), and the friction angle characteristic between them indicates that CRF-1 has a higher friction angle than CRF-2 (Barton's is denoted by residual friction angle).

4. Conclusions

Some general conclusions can be drawn from the results of this study:

(1) Shear interaction within CRF in underground mining practices can be divided into two types:
   (i) CRF-CRF interface, which can be assessed with direct shear testing of CRF interface, and
   (ii) CRF interparticle bonding, which can be assessed with triaxial testing of intact CRF.
(2) Direct shear testing to assess shear strength envelopes of CRF-CRF interfaces can be done through testing on prepared flat and smooth CRF-CRF surfaces with conversions and corrections, preferably using Barton's shear strength criteria.
(3) Two types of CRFs with the same aggregate size and distribution but different UCSs indicate insignificant differences either between their basic friction angles or basic friction angle plus the asperity angle. But, the residual friction angle between both may be different. Therefore, it is preferred to use the residual friction angle instead of the basic friction angle in any shear strength assessment of jointed CRF.
(4) There is an indication of CRF shear property where CRF is of different strengths but made from the same aggregate size and distribution: the stronger one tends to have a higher cohesion but a lower friction angle than the other.

Conflicts of interest

The authors wish to confirm that there are no known conflicts of interest associated with this publication and there has been no significant financial support for this work that could have influenced its outcome.

Acknowledgements

The authors would like to thank the University of Alberta Mining Department teams for their support and guidance. A grateful acknowledgement is given to the Indonesia Endowment Fund for Education scholarship (Grant No. 20151112014754/LPDP/2015) for the authors' financial assistance.

References

ASTM C192/C192M. Standard practice for making and curing concrete test specimens in the laboratory. ASTM International 2016:1–8.
ASTM C496/C496M. Standard test method for splitting tensile strength of cylindrical concrete specimens. ASTM International 2017;5. https://doi.org/10.1520/C0496.
ASTM D5607-16. Standard test method for performing laboratory direct shear strength tests of rock specimens under constant normal force. ASTM International 2016;4:1–9. https://doi.org/10.1520/D5607-16.
ASTM D7012-14. Standard test method for compressive strength and elastic moduli of intact rock core specimens under varying states of stress and temperatures. ASTM International 2014:1–9. https://doi.org/10.1520/D7012-14E01.
Bandis S, Lumsden AC, Barton N. Experimental studies of scale effects on the shear behaviour of rock joints. International Journal of Rock Mechanics and Mining Sciences & Geomechanics Abstracts 1981;18(1):1–21.
Barton N. Review of a new shear-strength criterion for rock joints. Engineering Geology 1973;7(4):287–332. https://doi.org/10.1016/0013-7952(73)90013-6.
Barton N. The shear strength of rock and rock joints. International Journal of Rock Mechanics and Mining Sciences & Geomechanics Abstracts 1976;13(9):255–79.
Barton N, Choubey V. The shear strength of rock joints in theory and practice. Rock Mechanics 1977;10(1/2):1–54. https://doi.org/10.1007/BF01261801.
Barton N, Bandis S. Effects of block size on the shear behavior of jointed rock. In: The 23rd U.S symposium on rock Mechanics (USRMS). American Rock Mechanics Association (ARMA); 1982. p. 739–60.
Barton N. Shear strength criteria for rock, rock joints, rockfill and rock masses: problems and some solutions. Journal of Rock Mechanics and Geotechnical Engineering 2013;5(4):249–61. https://doi.org/10.1016/j.jrmge.2013.05.008.
Barton N. Non-linear shear strength for rock, rock joints, rockfill and interfaces. Innovative Infrastructure Solutions 2016;1:30. https://doi.org/10.1007/s41062-016-0011-1.
Belem T, Benzaazoua M. Design and application of underground mine paste backfill technology. Geotechnical & Geological Engineering 2008;26(2):147–74. https://doi.org/10.1007/s10706-007-9154-3.
Emad MZ, Mitri HS, Henning JG. Effect of blast vibrations on the stability of cemented rockfill. International Journal of Mining, Reclamation and Environment 2012;26(3):233–43.
Hencher SR, Richards LR. The basic frictional resistance of sheeting joints in Hong Kong granite. Hong Kong Engineer 1982;11:21–5. https://www.researchgate.net/publication/284510099_The_basic_frictional_resistance_of_sheeting_joints_in_Hong_Kong_granite.
Marachi ND, Chan CK, Seed HB. Evaluation of properties of rockfill materials. Journal of the Soil Mechanics and Foundations Division 1972;98(1):95–114.
Mitchell RJ. Model studies on the stability of confined fills. Canadian Geotechnical Journal 1989;26(2):210–6. https://doi.org/10.1139/t89-030.
Muralha J, Grasselli G, Tatone B, Blümel M, Chryssanthakis P, Jiang YJ. ISRM suggested method for laboratory determination of the shear strength of rock joints: revised version. Rock Mechanics and Rock Engineering 2014;47(1):291–302. https://doi.org/10.1007/s00603-013-0519-z.
Newland PL, Allely BH. Volume changes during drained triaxial tests on granular materials. Geotechnique 1957;7(1):17–34. https://doi.org/10.1680/geot.1957.7.1.17.
Patton FD. Multiple modes of shear failure in rock. In: Proceedings of the 1st international conference on rock Mechanics. Lisbon: ISRM; 1966. p. 509–13.
Reschke AE. The use of cemented rockfill at Namew Lake mine. Manitoba, Canada. In: Minefill 1993;1993:101–8.
RocTest. HTC-HOEK triaxial cell. RocTest. 2017. p. 1–2. https://roctest.com/en/product/hoek-triaxial-cell.
Sepehri M, Apel DB, Hall RA. Prediction of mining-induced surface subsidence and ground movements at a Canadian diamond mine using an elastoplastic finite element model. International Journal of Rock Mechanics and Mining Sciences 2017a;100:73–82.
Sepehri M, Apel DB, Liu WV. Stope stability assessment and effect of horizontal to vertical stress ratio on the yielding and relaxation zones around underground

open stopes using empirical and finite element methods. Archives of Mining Sciences 2017b;62(3):653–69. https://doi.org/10.1515/amsc-2017-0047.
Shrestha BK, Tannant DD, Proskin S, Reinson J, Greer S. Properties of cemented rockfill used in an open pit mine. In: GeoEdmonton'08. Edmonton: The Canadian Geotechnical Society; 2008. p. 609–16.
Swan G. A new approach to cemented backfill design. CIM Bulletin 1985;78:53–8.
Talbot AN, Richart FE. The strength of concrete, its relation to the cement aggregates and water. University of Illinois at Urbana Champaign; 1923.
Yu TR, Counter DB. Backfill practice and technology at Kidd Creek mines. CIM Bulletin 1983;76:56–65.
Zhao J. Joint surface matching and shear strength part B. shear strength and JRC-JMC model. International Journal of Rock Mechanics and Mining Sciences 1997;34(2):179–85. https://www.sciencedirect.com/science/article/pii/S0148906296000630.

Bob A. Lingga obtained his MSc degree in Mining Engineering from University of Alberta, Canada and BSc degree in Mining Engineering from Bandung Institute of technology, Indonesia. Based on both of his degrees, his research focus and interests are related to backfills, geomechanics and geotechnics. In addition to current research activities, he used to work at a coal mining company and was familiar with operational activity in the field.